

## Coulomb explosion of diatomic molecules in intense XUV fields mapped by partial covariance

This content has been downloaded from IOPscience. Please scroll down to see the full text.

2013 J. Phys. B: At. Mol. Opt. Phys. 46 164028

(<http://iopscience.iop.org/0953-4075/46/16/164028>)

View [the table of contents for this issue](#), or go to the [journal homepage](#) for more

Download details:

IP Address: 160.45.66.60

This content was downloaded on 29/01/2015 at 12:20

Please note that [terms and conditions apply](#).

# Coulomb explosion of diatomic molecules in intense XUV fields mapped by partial covariance

O Kornilov<sup>1,10</sup>, M Eckstein<sup>1</sup>, M Rosenblatt<sup>1</sup>, C P Schulz<sup>1</sup>, K Motomura<sup>2</sup>,  
A Rouzée<sup>1</sup>, J Klei<sup>1</sup>, L Foucar<sup>3</sup>, M Siano<sup>4</sup>, A Lübcke<sup>1,11</sup>, F Schapper<sup>1,12</sup>,  
P Johnsson<sup>5</sup>, D M P Holland<sup>6</sup>, T Schlathölter<sup>7</sup>, T Marchenko<sup>8</sup>,  
S Düsterer<sup>9</sup>, K Ueda<sup>2</sup>, M J J Vrakking<sup>1</sup> and L J Frasinski<sup>4,10</sup>

<sup>1</sup> Max Born Institute, Max-Born-Strasse 2A, D-12489 Berlin, Germany

<sup>2</sup> Institute of Multidisciplinary Research for Advanced Materials, Tohoku University, Sendai 980-8577, Japan

<sup>3</sup> Max Planck Institute for Medical Research, D-69120 Heidelberg, Germany

<sup>4</sup> Blackett Laboratory, Imperial College London, SW7 2AZ, UK

<sup>5</sup> Department of Physics, Lund University, SE-22100, Lund, Sweden

<sup>6</sup> STFC Daresbury Laboratory, Warrington, Cheshire WA4 4AD, UK

<sup>7</sup> KVI Atomic and Molecular Physics, University of Groningen, Zernikelaan 25, NL-9747 AA Groningen, The Netherlands

<sup>8</sup> Laboratoire de Chimie Physique-Matière et Rayonnement, CNRS and UPMC, 11 rue Pierre et Marie Curie, F-75231 Paris, France

<sup>9</sup> Deutsches Elektronen-Synchrotron (DESY) Notkestrasse 85, D-22603 Hamburg, Germany

E-mail: [kornilov@mbi-berlin.de](mailto:kornilov@mbi-berlin.de) and [l.j.frasinski@imperial.ac.uk](mailto:l.j.frasinski@imperial.ac.uk)

Received 15 April 2013, in final form 14 June 2013

Published 13 August 2013

Online at [stacks.iop.org/JPhysB/46/164028](http://stacks.iop.org/JPhysB/46/164028)

## Abstract

Single-shot time-of-flight spectra for Coulomb explosion of N<sub>2</sub> and I<sub>2</sub> molecules have been recorded at the Free Electron LASer in Hamburg (FLASH) and have been analysed using a partial covariance mapping technique. The partial covariance analysis unravels a detailed picture of all significant Coulomb explosion pathways, extending up to the N<sup>4+</sup>–N<sup>5+</sup> channel for nitrogen and up to the I<sup>8+</sup>–I<sup>9+</sup> channel for iodine. The observation of the latter channel is unexpected if only sequential ionization processes from the ground state ions are considered. The maximum kinetic energy release extracted from the covariance maps for each dissociation channel shows that Coulomb explosion of nitrogen molecules proceeds much faster than that of the iodine. The N<sub>2</sub> ionization dynamics is modelled using classical trajectory simulations in good agreement with the outcome of the experiments. The results suggest that covariance mapping of the Coulomb explosion can be used to measure the intensity and pulse duration of free-electron lasers.

(Some figures may appear in colour only in the online journal)

<sup>10</sup> Authors to whom any correspondence should be addressed.

<sup>11</sup> Present address: Ecole Polytechnique Fédérale de Lausanne, Laboratoire de Spectroscopie Ultrarapide, Facultés Sciences de Base, CH- Lausanne, Switzerland.

<sup>12</sup> Present address: Carl Zeiss Laser Optics GmbH, 73447 Oberkochen, Germany.



Content from this work may be used under the terms of the [Creative Commons Attribution 3.0 licence](http://creativecommons.org/licenses/by/3.0/). Any further distribution of this work must maintain attribution to the author(s) and the title of the work, journal citation and DOI.

## 1. Introduction

Over the last few years, accelerator-based free-electron lasers (FELs) have emerged as new, large-scale user facilities, providing unprecedented XUV/x-ray fluences and intensities [1–4]. The considerable scientific and financial investment that underlies these developments is driven by applications in structural biology, where the possibility of determining the structure of tiny crystals or even non-crystalline materials

such as single macro-molecules and cells offers a promise substantially beyond the opportunities offered by contemporary synchrotron light sources [5, 6]. Initial results that have been obtained at the Linac Coherent Light Source at Stanford have already provided first glimpses of the potential of these techniques [7–10].

One question that has prominently surrounded these developments has been whether using an XUV or x-ray FEL allows recording diffraction patterns before the sample undergoes significant damage [5, 11]. Clearly, the massive x-ray induced ionization that accompanies an x-ray diffraction experiment will lead to destruction of the sample by a Coulomb explosion. However, if the x-ray pulse is short enough, the diffraction pattern can already be registered *before* the atoms move significantly. Hence, single particle x-ray diffractive imaging requires very short x-ray pulses, of the order of 10 fs duration, as well as an assessment of the sample stability against Coulomb explosion in the course of the ionization by intense x-ray beams.

Pilot studies of Coulomb explosion dynamics are often carried out with gas-phase molecular samples. In these experiments, the information about the evolution of the molecular structure on femtosecond timescales is encoded in the kinetic energy of ions ejected in the course of multiple ionization of the molecules. The dissociation dynamics in this regime is often termed ‘Coulomb explosion’, because the dissociation pathways of highly charged fragments can be well approximated by those of point charges. This approximation, however, does not hold for low-charge states, where the molecular electronic structure plays a significant role. We use the term ‘Coulomb explosion’ throughout the text with this important caveat in mind.

To unravel the information encoded in the kinetic energy, it is highly desirable to correlate the kinetic energy distribution of each ion with its initial position within the molecule. There exist a limited number of techniques with the potential to provide this information. The first of these is a measurement of ion–ion coincidences using a COLTRIMS-like detection system that makes use of delay-line detectors to record the 3D momentum distributions of ions that are formed [12]. Such a method was indeed used in some of the first experiments performed at the Free Electron LASer in Hamburg (FLASH), where N<sub>2</sub> molecules were exposed to intense ( $10^{13}$  W cm<sup>-2</sup>) 25 fs long FEL pulses centred at 28 nm wavelength ( $h\nu = 44$  eV) [13]. It was used later at the Spring-8 Compact SASE Source [14] to study multiple ionization dynamics of N<sub>2</sub> and O<sub>2</sub> exposed to intense 52 nm FEL pulses ( $h\nu = 24$  eV). The latter experiments showed that the multiple ionization of the molecules takes place not at the equilibrium bond length of the neutrals. A drawback of the use of coincident ion detection is that only one ion–ion pair or less can be tolerated per laser shot, making it very inefficient to use this technique at the currently available, low repetition rate FELs.

A second method that can be used is velocity map imaging (VMI) [15], where the kinetic energy of individual ( $m/Z$ ) ionic fragments can be measured by making use of a 2D detector that is gated to the arrival time of a particular ionic fragment, and where correlated ion pairs can be identified on

the basis of momentum matching. VMI was previously used in studies of IR-induced Coulomb explosions [16, 17]. It was recently applied to study the multi-photon ionization dynamics of atoms and molecules at FLASH [18, 19]. One problem that is encountered in VMI of Coulomb explosion at an x-ray FEL is the fact that the large kinetic energy release of highly charged fragments can lead to a situation where the arrival times on the detector of ions with slightly different ( $m/Z$ ) ratios begin to overlap. Under this condition, it becomes compulsory to measure the time-of-flight (TOF) of the partner ion(s) as well, in order to uniquely identify the fragmentation process.

Circumventing the above-mentioned drawbacks of ion–ion coincidence schemes and velocity map imaging, we present in this paper, as a third method, an improved covariance mapping technique, proposed some time ago [20, 21] and implemented recently at the FLASH FEL in Hamburg, where we have used intense FEL pulses at 91 eV (13.7 nm) to observe dissociative ionization and Coulomb explosion of two diatomic molecules, N<sub>2</sub> and I<sub>2</sub>. The improvement over the standard covariance mapping consists in using the *partial* covariance, i.e. the part of covariance that is independent of XUV pulse energy fluctuations, which allows us to increase the counting rate substantially. Compared to the aforementioned ion–ion coincidence measurements, the experiments could be performed while working under conditions where thousands of molecules are ionized per laser shot, clearly precluding the possibility of a coincidence analysis. Compared to the VMI experiments, the covariance measurement allowed the de-convolution and unique characterization of numerous overlapping contributions in the arrival time distribution on the detector.

The outcome of our covariance analysis is a determination of the kinetic energy release accompanying the formation of specific charged ion pairs. For the case of N<sub>2</sub>, where only valence ionization is involved, these kinetic energy distributions are compared to the results of Monte Carlo classical trajectory simulations. The comparison shows excellent agreement both in charge state distributions and in momentum distributions of individual Coulomb explosion channels up to the highest observed N<sup>4+</sup>–N<sup>5+</sup> channel. For the case of iodine, the covariance maps reveal individual channels up to the I<sup>8+</sup>–I<sup>9+</sup> channel.

## 2. Experimental methods

Figure 1 shows the experimental setup that was used at the BL2 beam line of the FLASH FEL in Hamburg. The FEL was operated at a bunch repetition rate of 10 Hz and at a photon energy of 91 eV. Each bunch consisted of 30 pulses with a 10  $\mu$ s inter-pulse separation. The pulse energy envelope peaked near the middle of the bunch with the pulse energies ranging from 14 to 71  $\mu$ J and considerable energy fluctuations from bunch to bunch. The FEL beam was focused using an  $f = 2$  m ellipsoidal mirror, resulting in a focal spot of about 15  $\mu$ m in diameter [22]. Estimating the FEL pulse duration to be approximately 100 fs (full-width at half-maximum, FWHM), typical focused intensities of  $10^{14}$  W cm<sup>-2</sup> were thus obtained,

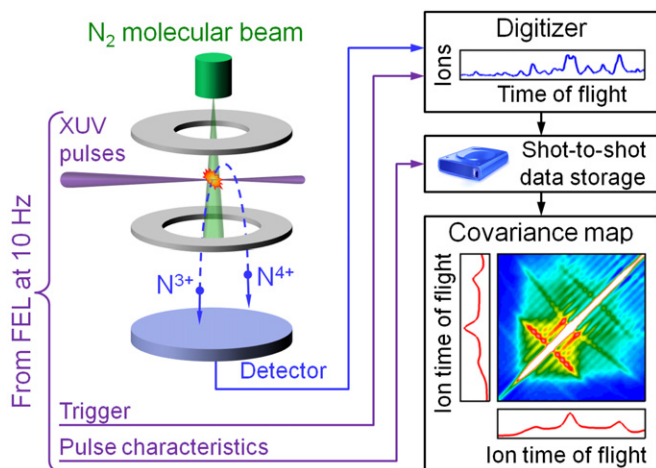


**Figure 1.** Sketch of the experimental setup. XUV pulses are focused on a molecular sample. The molecules are ionized and dissociate. Ion fragments are accelerated towards a detector by a static electric field. At each laser shot, a time-of-flight (TOF) spectrum of the ions is recorded and its contribution to a covariance map is calculated using the FEL pulse characteristics.

allowing the molecules to be multiply ionized and thereby inducing a Coulomb explosion.

The FEL pulses were focused onto a skimmed pulsed molecular beam that passed through the active region of a VMI spectrometer [15]. In the present experiments, the VMI instrument was operated not in the VMI mode, but in a TOF mode. The potentials applied to the repeller and extractor electrodes of the VMI spectrometer created a  $50 \text{ V cm}^{-1}$  extraction field at the entrance of the 10 cm long VMI drift region, and thus guided the fragment ions towards a microchannel plate (MCP) + phosphor screen detector. A fast digitizer (Acqiris U1092) recorded the electron current at the phosphor screen via a capacitive coupling. A single waveform was recorded for each complete FEL bunch at a sampling period of 1 ns. In the first step of data analysis, this waveform was separated into single-shot waveforms corresponding to each individual FEL pulse in the bunch, which were subsequently used to construct the ion TOF spectra and covariance maps. Another channel of the digitizer recorded the relative pulse energy of the individual FEL pulses, as measured by a photodiode. The digitized ion and photodiode waveforms were stored locally for each laser shot in a custom local memory address format. The absolute pulse energies and further FEL parameters, such as the bunch frequency and the wavelength, were recorded on a separate facility network.

The extraction voltages used in the present experiment are rather low (on the order of 200 V) in order to spread the arrival times of the ions that were produced over several  $\mu\text{s}$ . However, these low extraction voltages lead to significant variation in the gain of the MCP detector with the charge state of the ion. Therefore, quantitative comparison of the  $\text{N}_2$  data with calculations presented below requires corrections of the recorded ion signals for these variations. The expressions for secondary electron yields by various ions (proportional to the detected signal) are known from the literature [23]. The secondary electron yields are typically expressed as a sum of the kinetic emission contribution due to the ion velocity and

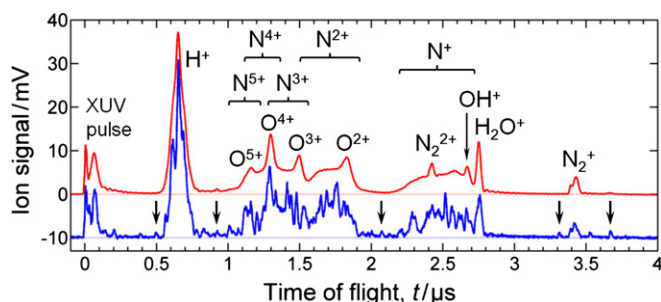


**Figure 2.** TOF spectrum of ions from Coulomb explosion of  $\text{N}_2$ , averaged over all recorded FEL shots (red) and a single-shot spectrum (blue, shifted by  $-10 \text{ mV}$ ) showing individual ion hits (marked with arrows) where the signal is low. In the regions of high ion signal the individual pulses overlap, which excludes the use of coincidence techniques. The Coulomb explosion leads to a broadening of the  $\text{N}^{n+}$  atomic ion islands and, consequently, a mutual overlap of these islands. Several relatively sharp peaks resulting from the ionization of background gas can be seen as well. The combination of both observations effectively prevents a measurement of the kinetic energy of the  $\text{N}^{n+}$  atomic ion peaks on the basis of this TOF spectrum.

the potential emission contribution due to the recombination of conduction-band electrons with the highly charged ions. The expression for kinetic emission by nitrogen ions was taken from [24]. Ions with charges higher than 3+ may invoke potential emission at the surface of the MCP and thus require additional corrections taken from [25, 26]. The combined correction divisors used here were 0.089, 0.23, 0.54, 2.14 and 3.53 for charge states 1+ to 5+, respectively. Similar data are not readily available for iodine ions and, since for iodine no quantitative comparison is attempted in this work, these detection efficiency corrections were not implemented.

An ion TOF spectrum resulting from ionization and Coulomb explosion of  $\text{N}_2$  is shown in figure 2. The measurement that is shown was averaged over 378 219 FEL shots. At zero TOF, electromagnetic noise coming from the machine operation is visible. Molecular ions resulting from ionization of  $\text{N}_2$  show up in the form of small parent molecular ion peaks,  $\text{N}_2^+$  and  $\text{N}_2^{2+}$ . In addition, atomic ions  $\text{N}^{n+}$  ( $n = 1-5$ ) resulting from the dissociation and Coulomb explosion of multiply ionized  $\text{N}_2$  are clearly visible in the form of broad islands that span a considerable TOF range. This is a direct result of the substantial kinetic energy release that occurs in the Coulomb explosion and leads to overlaps between contributions from fragment ions with a different ( $m/Z$ ) ratio in the TOF. This overlap makes it impossible to analyse the kinetic energies of the Coulomb explosion fragments in a direct manner.

Note that the peak labelled  $\text{N}^+/\text{N}_2^{2+}$  contains contributions from both non-dissociative double ionization (without kinetic energy release) and the formation of energetic  $\text{N}^+$  ions originating from one or more Coulomb explosion channels. In addition to peaks originating from the ionization and Coulomb explosion of  $\text{N}_2$ , the TOF spectrum contains prominent peaks from ionization of water that do not originate from the molecular beam but that accumulate from the ionization of background gas during the passage of the FEL beam between the VMI electrodes.

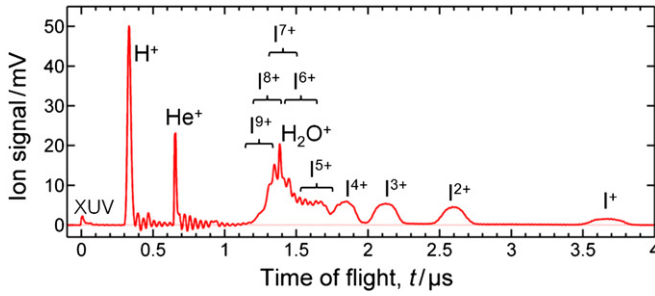


**Figure 3.** TOF spectrum of ions from Coulomb explosion of  $I_2$ . While the peaks corresponding to the detection of  $I^+$  to  $I^{4+}$  have only a modest overlap with the detection of other ( $m/Z$ ) peaks, the detection of  $I^{5+}$  to  $I^{9+}$  is severely compromised by overlapping contributions from the neighbouring charge states and from the ionization of background gas in the experimental chamber. Filtering out these contributions requires a covariance analysis.

Figure 2 clearly shows that in the presence of extensive multiple ionization and Coulomb explosion, uncorrelated measurements along a single TOF-axis contain only limited information. This is even more apparent when looking at figure 3, where a similar average TOF spectrum is presented for the case of  $I_2$ . The islands corresponding to the ions from  $I^+$  to  $I^{4+}$  can clearly be separated; however, the islands for charges from  $I^{5+}$  to  $I^{9+}$  are fully merged together. This is precisely where the covariance analysis that will be used here will prove its usefulness.

### 3. Data analysis method

The momenta of two ions that are ejected from the same parent diatomic molecule are equal but opposite. The detection events for these two fragments are thus correlated. To reveal these correlations we use a method of statistical data analysis called ‘covariance mapping’. The standard version of this technique has been published before [20]. Briefly, the method treats ion signals in individual TOF channels as random variables and calculates the covariance for each pair of these variables producing a map of ion TOF correlations (see figure 1). These correlations arise from fluctuations in the number of Coulomb explosion events from pulse to pulse. Pairs of variables corresponding to different times of flight are necessarily correlated, because recorded fragments originate from the same molecules. In practice, the single-shot ion waveforms, shown in figure 2, are considered to be row vectors  $\mathbf{X} = X(t_x)$  representing the ion signal  $\mathbf{X}$  at discretized TOF  $t_x$ . Each vector is also transposed into a column vector,  $\mathbf{Y} = \mathbf{X}^T$ . The two vectors are multiplied, giving a matrix indexed by two discrete TOFs  $\mathbf{YX} = Y(t_y)X(t_x)$ . This matrix, averaged over many laser shots, can be visualized as a map  $\langle \mathbf{YX} \rangle$ . Figure 4(a) shows such a map for the case of the  $N_2$  measurements (described in the previous section) averaged over all 378 219 FEL shots. In a similar way, the waveforms are averaged first and then combined in a matrix product  $\langle \mathbf{Y} \rangle \langle \mathbf{X} \rangle$ , which gives the map shown in figure 4(b). Subtracting the two maps,

$$\mathbf{cov}(\mathbf{Y}, \mathbf{X}) = \langle \mathbf{YX} \rangle - \langle \mathbf{Y} \rangle \langle \mathbf{X} \rangle, \quad (1)$$

gives the covariance map as shown in figure 4(c). Correlations of signals in samples of different TOFs show up as non-zero

regions in the covariance map. The relatively strong diagonal line in the covariance map in figure 4(c) is an autocorrelation line, which reflects the simple fact that an ion signal recorded as  $X(t_x)$  is the same as the signal  $Y(t_y = t_x)$ . The autocorrelation line is equal to the variance of the TOF signal:  $\mathbf{cov}(\mathbf{Y}, \mathbf{Y}) = \mathbf{var}(\mathbf{Y})$ . Faint ion momentum correlation lines start to be visible in figure 4(c) approximately perpendicular to the autocorrelation line. The orientation of these lines is given by the momentum conservation law: if one fragment of the exploding molecule moves towards the detector thereby reducing its TOF, the other fragment is necessarily moving in the opposite direction and thus—after being turned around by the extraction electric field—will be recorded at later times.

The map in figure 4(c) is still overwhelmed by unwanted correlations, represented by vertical and horizontal lines or bands. These artefacts are mainly due to fluctuations in the FEL pulse energy, but to some extent can also appear due to fluctuation of other experimental parameters, such as pulse shape, pulse duration or sample density. These fluctuations correlate every ion with every other ion, simply because an increase in pulse energy produces more ions of every kind. To remove these correlations we calculate the coefficient of *partial* covariance using the expression [27]

$$\mathbf{pcov}(\mathbf{Y}, \mathbf{X}; I) = \mathbf{cov}(\mathbf{Y}, \mathbf{X}) - \mathbf{cov}(\mathbf{Y}, I)\mathbf{cov}(I, \mathbf{X})/\mathbf{cov}(I, I), \quad (2)$$

where  $I$  is the FEL pulse energy and  $\mathbf{cov}(\mathbf{Y}, I)$ ,  $\mathbf{cov}(I, \mathbf{X})$  are the column and row vectors of covariance coefficients, respectively. Effectively, equation (2) compensates the standard covariance map (figure 4(c)) for the uninteresting correlations via  $I$ , represented by the second term on the right-hand side in equation (2) (see figure 4(d)). Subtracting the two maps produces a partial covariance map (figure 4(e)), where the ion momentum correlation lines are clearly visible, although somewhat obscured by periodic modulation due to detector ringing.

The application of equation (2) shown in figure 4(e) seems to undercompensate for the effects of the FEL pulse energy variations, because the co-variant momentum-matched atomic ion contributions sit on top of a positive background. Furthermore, the molecular  $N_2^{2+}$  ion carves out a negative valley in the 2D plot shown in figure 4(e). These residual correlations can be induced by the fluctuating density of  $N_2$  molecules in the pulsed molecular beam or by the fluctuating duration of the FEL pulses. We found that introducing a factor in front of the compensation term in equation (2) and manually varying it helps to significantly reduce the background in the region where the co-variant momentum-matched atomic ions are detected. The best result is achieved for the factor of 1.1, which however deepens the negative valleys in the region where molecular ions are detected (see figure 4(f)). Nevertheless, we use this ad hoc method, which allows us to suppress the background in the region of interest. A similar map for  $I_2$  is presented in figure 5.

The variation in the TOF with the initial ion momentum component parallel to the drift tube axis has been simulated using the SIMION software. The excellent agreement between the simulated and observed TOF for zero kinetic energy

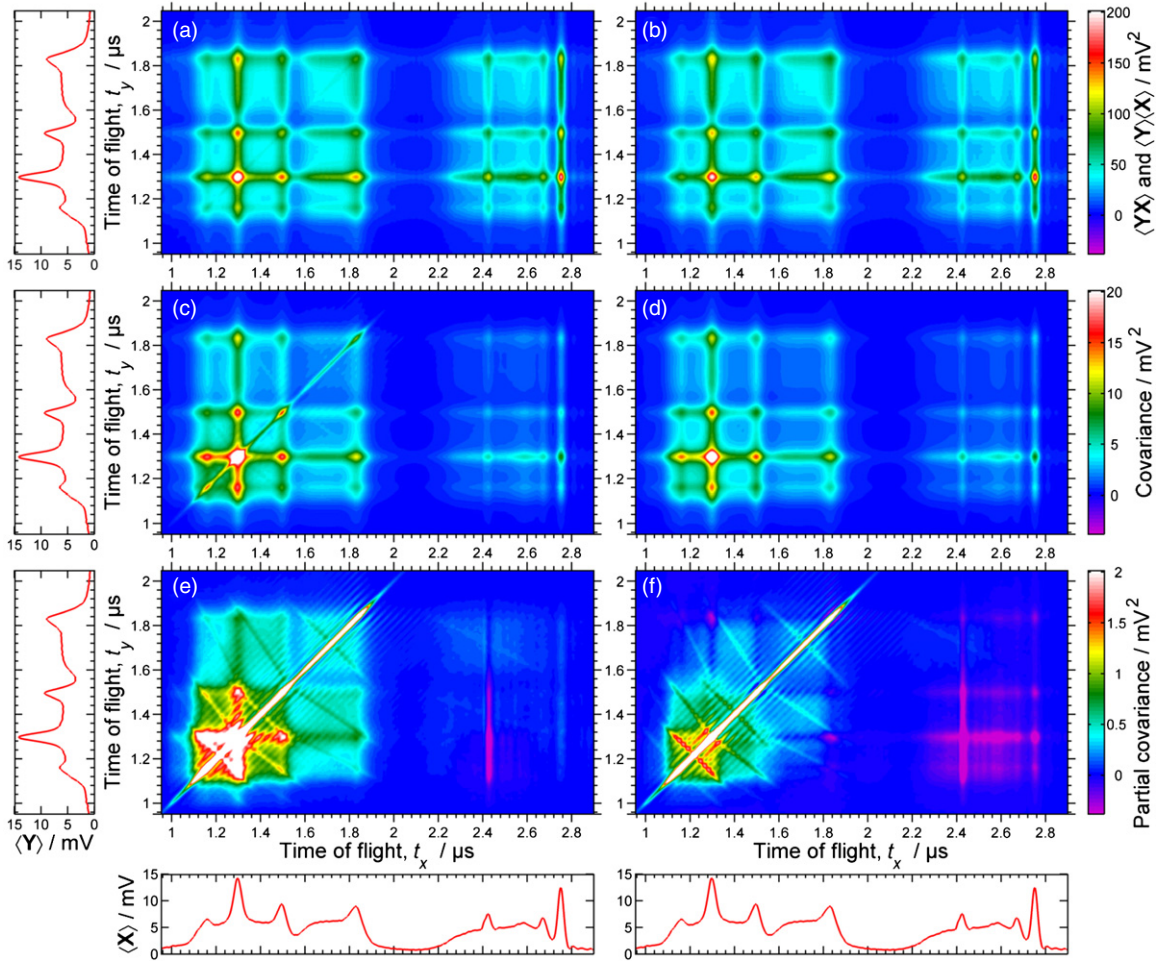


**Figure 4.** Steps in resolving the ion momentum correlations in Coulomb explosion of  $N_2$  molecules. The FEL pulse has an average energy of  $48 \mu\text{J}$  and an expected duration of approximately  $100 \text{ fs}$ . From the average product of the TOF spectra,  $\langle YX \rangle$  (a), the product of the average spectra,  $\langle Y \rangle \langle X \rangle$  (b), is subtracted, thereby giving the standard covariance map,  $\text{cov}(Y, X)$  (c) (note the change in the colour scale). Next, correlations from FEL pulse to pulse fluctuation in energy,  $\text{cov}(Y, I)$   $\text{cov}(I, X)/\text{cov}(I, I)$  (d), are subtracted giving a partial covariance map,  $\text{pcov}(Y, X; I)$  (e). Further background suppression (f) can be achieved by subtracting 110% of the correction factor.

molecular ions gives us confidence that the kinetic energy scales are accurate to 5%. This agreement allows us to extract detailed momentum distributions for each of the individual Coulomb explosion channels visible on the maps. Some of these distributions are presented later in figure 9. Experimental values of the maximum kinetic energy of fragments are given in tables 1 and 2 for those channels where they could be reliably extracted.

#### 4. Ionization and Coulomb explosion dynamics

To gain a deeper understanding of the dynamics of molecular Coulomb explosion in short XUV pulses, simulations were carried out for the case of  $N_2$  ionization. The simulations employ classical trajectories to calculate the kinetic energies of the emerging ionic fragments. The molecules are exposed to an intense XUV pulse and are sequentially singly ionized at moments that are chosen using a Monte Carlo procedure based on the ionization cross sections and instantaneous pulse intensity. The simulations neglect single-photon double ionization including formation of doubly charged atomic ions on the first ionization step, which constitute only about 0.5% at

**Table 1.** Maximum kinetic energy (KE) per fragment for  $N_2$  extracted from figure 4(f) and from simulation; effective internuclear distances for all observed charge pairs. Statistical uncertainties in the last digits are given in parentheses (two sigma); however, larger systematic errors may not be excluded.

Charge pair	Experimental KE/eV	Simulated KE/eV	Eff. distance/Å
1-1	3.3(9)	6.6	2.2(6)
1-2	7.2(6)	8.3	2.0(2)
1-3	8.7(11)	10.0	2.5(3)
1-4	–	11.3	–
1-5	–	12.6	–
2-2	10.5(2)	10.8	2.8(1)
2-3	13.4(4)	12.8	3.2(1)
2-4	17.2(6)	14.5	3.4(1)
2-5	–	15.5	–
3-3	20.0(5)	14.9	3.2(1)
3-4	25.0(4)	17.3	3.5(1)
3-5	–	19.7	–
4-4	27.2(1)	20.0	4.23(2)
4-5	27.5(6)	23.5	5.2(1)

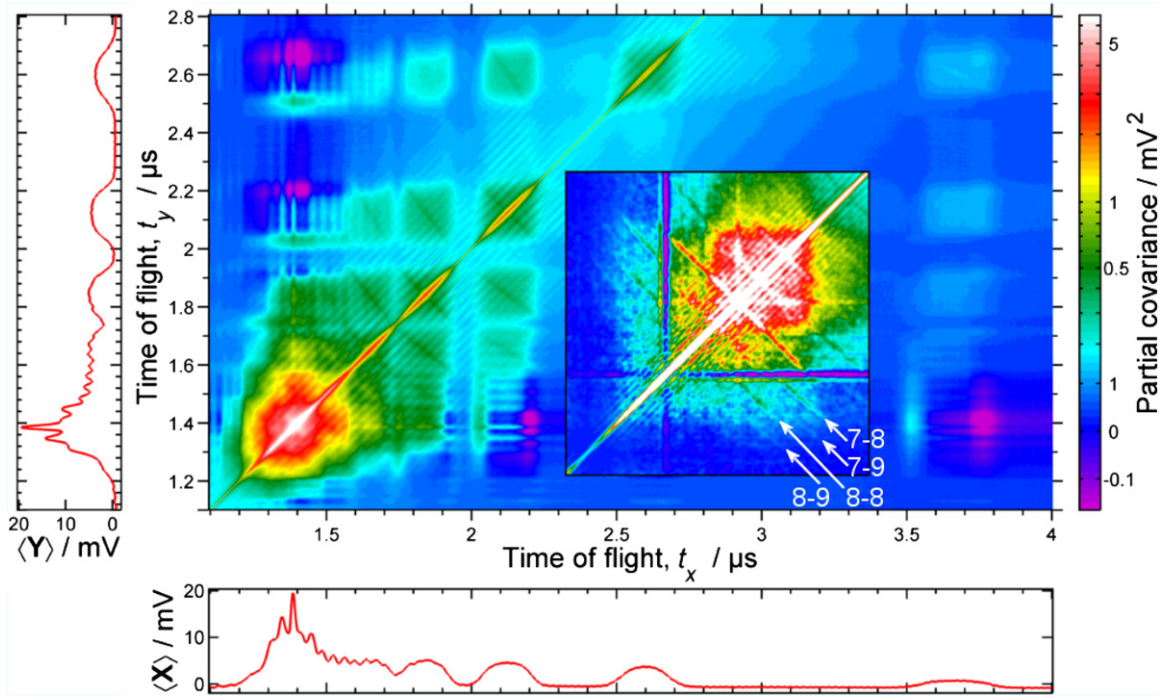


**Figure 5.** A partial covariance map of  $\text{I}_2$  fragmentation constructed from TOF data recorded at FLASH. The FEL pulse has an average energy of  $27 \mu\text{J}$  and an expected duration of approximately 100 fs. The inset shows correlations of the high charges recorded with the acceleration field of the spectrometer reduced by a factor of 4. The inset TOF range is 2.0–3.4  $\mu\text{s}$ . Fragmentation channels 7–8, 7–9, 8–8 and 8–9 are indicated by arrows. For better visibility, the inset is plotted with a nonlinear colour scale.

**Table 2.** Maximum kinetic energy (KE) per fragment for  $\text{I}_2$  extracted from figure 5 and effective internuclear distances for all observed charge pairs. Statistical uncertainties in the last digits are given in parentheses (two sigma); however, larger systematic errors may not be excluded.

Charge pair	Fragment KE/eV	Eff. distance/ $\text{\AA}$
1–1	2.5(1)	2.9(1)
1–2	3.2(2)	4.5(2)
2–2	4.3(1)	6.7(2)
2–3	7.0(3)	6.2(3)
2–4	7.8(4)	7.4(4)
3–3	11.6(3)	5.6(1)
3–4	13.9(2)	6.2(1)
4–4	18.5(5)	6.2(2)
6–6	44(3)	5.8(3)
6–7	54(2)	5.6(2)
7–7	69(3)	5.1(2)
8–8	88(8)	5.2(5)

this photon energy [28]. Only valence ionization is included in the simulation, because Auger and Coster–Kronig transitions are closed for nitrogen atoms at this photon energy. For this reason, the simulation could not be extended to the case of  $\text{I}_2$ , where Auger relaxation of the 4d orbitals plays a major role.

The molecules are treated as pairs of atoms located at a given distance from each other. The initial separation is changed by the Coulomb explosion dynamics. The ensemble of molecules in the experiment is at room temperature. However, owing to the large vibrational quantum of the nitrogen molecule, population of vibrational states above the ground state can be neglected. Thus the internuclear distances in the simulation are sampled from a probability distribution corresponding to the zero-point vibrational wavefunction of

**Table 3.** Cross sections at 91 eV photon energy and ionization potentials of N atoms and ions used in the simulation [29].

Initial configuration	Final configuration	Cross section/Mb	Ionization potential/eV
$2s^2 2p^3$	$2s^2 2p^2$	0.79	13.0
$2s^2 2p^3$	$2s^1 2p^3$	0.54	25.3
$2s^1 2p^3$	$2s^1 2p^2$	0.89	27.5
$2s^2 2p^2$	$2s^2 2p^1$	0.65	29.0
$2s^2 2p^2$	$2s^1 2p^2$	0.61	39.7
$2s^1 2p^3$	$2s^0 2p^3$	0.33	41.9
$2s^0 2p^3$	$2s^0 2p^2$	0.99	44.0
$2s^1 2p^2$	$2s^1 2p^1$	0.74	45.9
$2s^2 2p^1$	$2s^2 2p^0$	0.42	48.1
$2s^2 2p^1$	$2s^1 2p^1$	0.71	56.6
$2s^1 2p^2$	$2s^0 2p^2$	0.38	58.5
$2s^0 2p^2$	$2s^0 2p^1$	0.85	64.8
$2s^1 2p^1$	$2s^1 2p^0$	0.48	67.4
$2s^2 2p^0$	$2s^1 2p^0$	0.85	75.9
$2s^1 2p^1$	$2s^0 2p^1$	0.44	77.4
$2s^0 2p^1$	$2s^0 2p^0$	0.55	88.3
$2s^1 2p^0$	$2s^0 2p^0$	0.00	98.3

the molecule (equilibrium distance of 1.1  $\text{\AA}$ ). This sampling leads to variations in the initial conditions for the explosion trajectories and correctly reproduces the distribution of final energies. The cross sections for ionization from each of the shells are taken from [29] and are summarized in table 3 together with the ionization potentials (IPs). In the simulation, the IPs of the molecules dynamically depend on the instantaneous charge states and on the separation between the two atoms. The IP of an individual atom is calculated as the sum of the IP of an isolated atom and the Coulomb attractive potential of the second atom in the pair. Since the

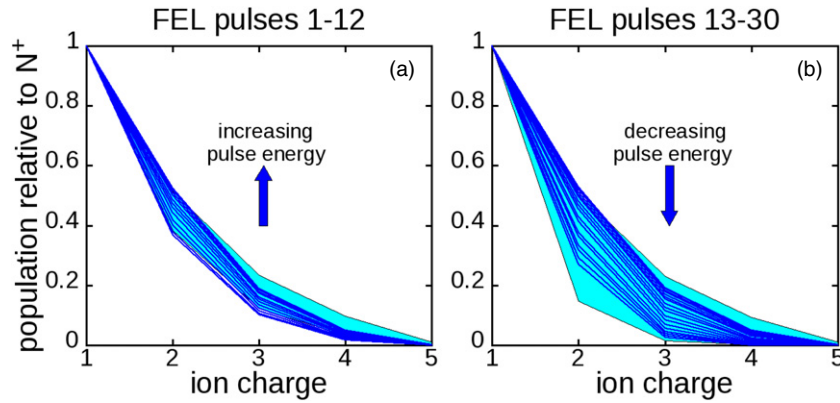


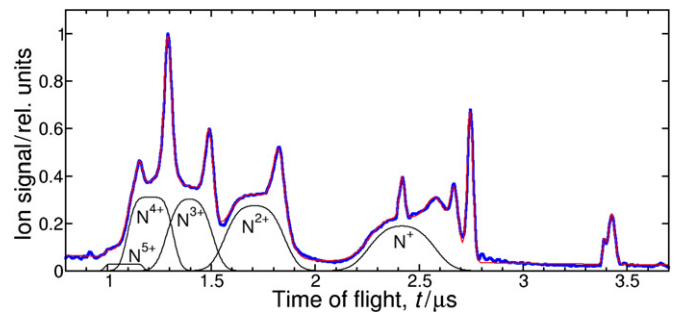
**Figure 6.** Charge state distributions of  $N^{n+}$  as a function of the FEL pulse energy. The experimental distributions are plotted as blue lines, normalized to the yield of singly charged  $N^+$  ions. (a) Distributions for the first part of the FEL bunch train, with the average FEL pulse energy increasing from 48 to 71  $\mu\text{J}$ . (b) Distributions for the second part of the FEL bunch train, with the average FEL pulse energy decreasing from 71 to 14  $\mu\text{J}$ . Results of the simulation are shown as cyan areas shaded between distributions with the highest and lowest pulse energies.

latter contribution changes in the course of the explosion, the IP of the atom is time dependent. The only molecular effect taken into account in the present simulations is charge migration from one atom to the other in a  $N^{2+}-N$  pair, leading to the formation of an  $N^+-N^+$  pair and initiating the Coulomb explosion. The probability of this migration is taken to be 100%. This assumption neglects the formation of stable  $N_2^{2+}$  molecules, which constitute less than 10% of all double-ionization events (estimated from the data in figure 2).

In the simulation, the XUV light of the FEL is represented by a Gaussian pulse with a temporal FWHM of 100 fs. Recording single-shot pulse energies in the experiment along with the TOF traces allows for the construction of a pulse energy distribution. The XUV pulse energy in the simulation was randomly sampled from this experimentally determined distribution. Essentially, each molecule in the ensemble interacts with a pulse of different energy. Averaging of the laser intensity over the focal volume is treated in a similar way. The radial intensity distribution is assumed to have a Gaussian shape with the FWHM of 14  $\mu\text{m}$ . This value lies within the uncertainty of the focus size quoted for this beam line [22] and is consistent with the observed charge state distributions. In [22], the Rayleigh length of the XUV focus is estimated to be about 10 mm. This is much longer than the width of the molecular beam (2 mm) and therefore the variation in the XUV intensity along the XUV beam is neglected. The simulation is carried out in a time window of 400 fs with the XUV pulses centred in this window.

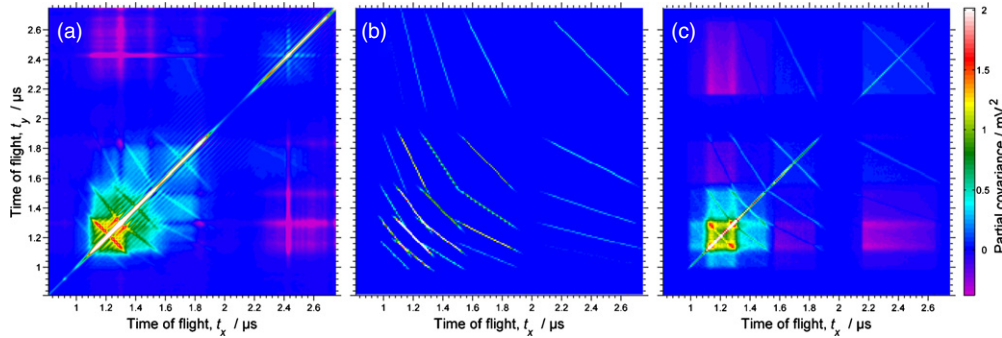
## 5. Results of the simulation and comparison with the experiment for the case of $N_2$

Figure 6 presents a comparison of the normalized charge state distributions of  $N^{n+}$  ions extracted from the experimental data with those simulated using the method described in section 4. In producing this figure, average TOF spectra recorded for each of the 30 pulses of the FEL bunch were fitted using a least-squares fit to a function representing the features in the TOF identified in figure 2. Each of the background peaks was represented by a Gaussian with a fixed position, and a



**Figure 7.** Extraction of the charge state distributions of  $N^{n+}$  fragments from the average TOF spectra of specific pulses in the 30 pulse long FEL bunch. The average TOF spectrum of the tenth pulse (blue) is fitted to a model distribution (red). Below are model curves corresponding to charge fragments  $N^+-N^{5+}$  (black).

variable width and area. The broad peaks resulting from the Coulomb explosion of  $N_2$  were represented as products of two error functions symmetrically positioned around the fixed TOF of the corresponding ion with zero kinetic energy. Widths and heights of the broad peaks were allowed to vary giving a rounded trapezoidal shape. The results of the fitting procedure presented in figure 7 allowed us to extract relative ion yields for all five charged states produced in the Coulomb explosion of  $N_2$ . The extracted yields were corrected for the detection efficiency of individual ions, as described in section 2. The data are plotted in figures 6(a) and (b). Figure 6(a) contains charge state distributions for pulses 1–12, for which the average pulse energy was increasing from 48 to 71  $\mu\text{J}$ . Figure 6(b) contains the remaining distributions for pulses 13–30, for which the average pulse energy was decreasing from 71 to 14  $\mu\text{J}$ . The simulations for these pulse energies are shown as cyan shaded areas with the top and bottom edges corresponding to the highest and lowest pulse energies, respectively. The agreement between the experimental and simulated charge state distributions is quite satisfactory given the number of assumptions built into the simulation and the relative complexity of the multi-photon ionization. Discrepancies of the order of 30–50% for some charge states can be attributed



**Figure 8.** Comparison of the experimental and simulated covariance maps. (a) Experimental partial covariance map (same as figure 4(f)). (b) Simulated coincidence map, which avoids most of the artefacts present in the covariance maps. (c) Simulated partial covariance map showing the effect of intensity correlations similar to that observed experimentally.

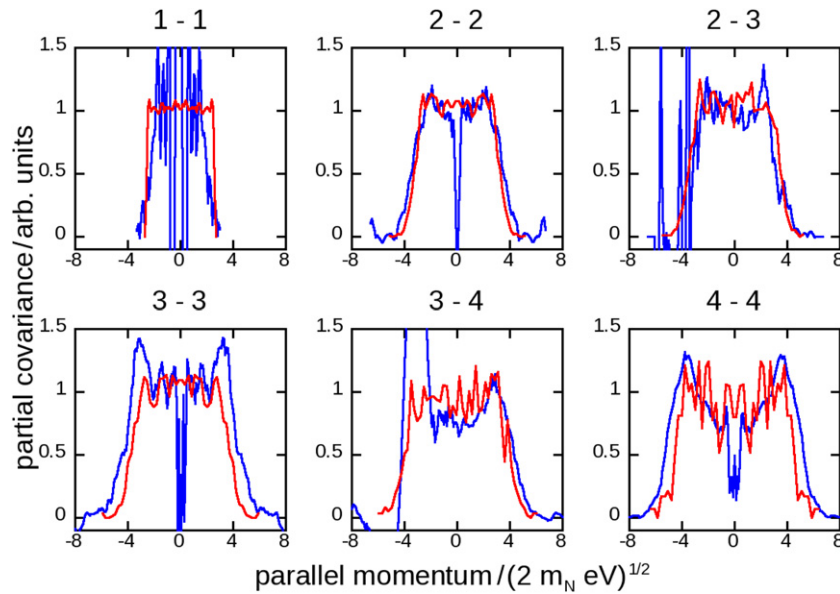


**Figure 9.** Comparison of charge state-selected momentum distributions extracted from the experimental partial covariance map of  $N_2$  fragments (blue) and obtained from the simulations (red). The corresponding charge pairs are indicated in the header of each part of the figure. The distributions are individually scaled for better visibility. The units of the parallel momentum such as squaring the value gives kinetic energy of the fragment in eV.

to uncertainties in the detection efficiencies and to detector saturation.

Further agreement between the experiments and simulations is demonstrated in figure 8. While figure 6 features integral characteristics of the Coulomb explosion, figure 8 demonstrates the power of the covariance mapping to extract information about fine details of the molecular dynamics. The experimental map in figure 8(a) (the same map as in figure 4(f)) is compared to the simulated coincidence map in figure 8(b). The coincidence map is constructed based on direct counting of the ionic pairs in the simulation, i.e. assuming only one pair per laser shot, and thus does not show any of the artefacts (such as the diagonal autocorrelation ridge) appearing in covariance maps. In contrast, figure 8(c) demonstrates the simulated *partial* covariance map directly comparable to figure 8(a). This map was calculated assuming that each laser shot illuminates on average 1000 molecules and constructing the map using equations (1) and (2).

The agreement between the experiment and the simulations is very satisfactory. This is emphasized in figure 9

and in table 1. Figure 9 shows the momentum distributions for Coulomb explosion channels by reading the map along the correlation ridges (lines visible in the covariance maps). As mentioned in section 3, the covariance islands are superimposed upon a background originating from residual correlations not eliminated by the partial covariance mapping procedure. To correct for this background, the map was sampled along the bottom of the correlation ridge (where it appears to be merging to the background) and these spectra were subtracted from the signal on top of the ridge. In this way, most of the remainder of the uninteresting correlations was removed. In figure 9, the distributions extracted for selected nitrogen ion pairs with charges 1–1, 2–2, 2–3, 3–3, 3–4 and 4–4 are compared with the same distributions extracted from the simulations. The shapes of most distributions match very well, except for a few artefacts (in the centre for symmetric channels and on the left for asymmetric ones) appearing due to the autocorrelation line, which cannot completely be corrected for. These artefacts do not prevent further analysis. The agreement between the experiment and the simulation can be

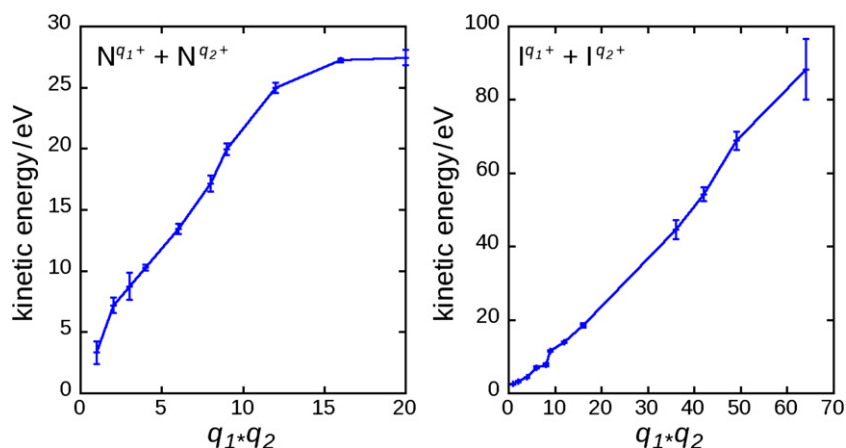


**Figure 10.** Maximum kinetic energy release per fragment plotted as a function of the product of two fragment charges in each channel. The saturation of the curve for nitrogen suggests fast explosion competing with the duration of the FEL pulse (100 fs), while for the heavier iodine atoms the explosion is slower, as expected.

readily seen in table 1, which lists maximum kinetic energies of fragments extracted from the widths of the distributions.

The strongest deviation is observed for the 1–1 case, where the experimental distribution has a bell shape, while the simulation predicts an almost square shape. This discrepancy can be attributed to the assumption taken in the simulation, that there is no dissociation or vibrational excitation of the singly charged nitrogen molecules,  $N_2^+$ . This assumption is certainly incorrect. Such a dissociation would lead to slowly moving singly charged  $N^+$  ions, which are probably recorded in the experiment.

## 6. Discussion

The application of partial covariance mapping to multi-photon ionization by intense XUV pulses demonstrates the power of this technique to extract fine details of the Coulomb explosion dynamics. Thus, in the partial covariance maps of  $N_2$  and  $I_2$ , it is possible to discern 12 and 22 individual Coulomb explosion channels, respectively. Tables 1 and 2 list maximum fragment kinetic energies for the most populated explosion channels. To refer the extracted values to molecular geometry, they are converted to effective distances between the two charged fragments (also listed in the tables) using the Coulomb law. By comparing the two progressions, it is immediately apparent that, in both cases, the effective distances are larger than the equilibrium bond lengths of 1.1 Å and 2.7 Å, in  $N_2$  and  $I_2$ , respectively. This is to be expected because the effective distances extracted in this way give a lower bound: kinetic energy acquired by the fragments at preceding ionization stages is neglected. For the case of nitrogen, the effective distances monotonically increase from 2.2 to 5.2 Å indicating fast explosion of the molecule initiated by the first ionization steps. In contrast, for the heavier iodine atoms, the values quickly increase from about 3 Å to about 6.5 Å for low-charge channels and then remain more or less constant for the high-charge channels. The same information is presented in figure 10 as a plot of maximum observed kinetic energy versus the product of two charges in each channel. Assuming the Coulomb potential ( $\propto q_1 q_2 / r$ ), if each explosion were to

start from the same internuclear distance, such plots would show straight lines. This is the case for iodine, but is drastically different for nitrogen, where the kinetic energy seems to saturate for higher charges. This suggests that the  $I_2$  dynamics are slow, while  $N_2$  explodes on a timescale that is faster than the FEL pulse duration. Note, however, that the slope of the line for iodine does not correspond to its equilibrium interatomic distance.

Given the experimental intensities of  $10^{14} \text{ W cm}^{-2}$ , we assume that only sequential ionization processes are possible. In this case, at 91 eV photon energy only valence ionization is allowed in nitrogen. This means that for each observed charge fragment, the number of absorbed photons is equal to the charge state. Hence, for the highest observed channel,  $N^{4+}$ – $N^{5+}$ , absorption of nine photons within the 100 fs pulse envelope is required. The average number of absorbed photons is, of course, lower and constitutes about three photons per molecule, as can be estimated from charge state distributions in figure 6. In the case of iodine, Auger processes to the 4d shell are involved in the early ionization stages, before the IP of this shell increases above the photon energy at  $I^{3+}$ . Thus, absorption of about 13 photons is sufficient to reach the highest observed  $I^{8+}$ – $I^{9+}$  channel.

The simulations presented in the previous section may serve as a good starting point for understanding molecular effects in the Coulomb explosion, as well as for the characterization of unknown parameters in the experiment. As an example, figure 11 shows variations in the width of the momentum distributions for 1–1, 2–2, 3–3 and 4–4 nitrogen ion pairs for a range of XUV pulse conditions. These widths correspond to the maximum kinetic energy observed in the Coulomb explosion event, because an explosion with a randomly oriented axis and constant energy would produce a square parallel momentum distribution with a width determined by the absolute value of the maximum momentum parallel to the TOF axis. Figure 11(a) shows the variation in the width with the average pulse energy (over the range covered in figure 6). It is readily apparent that the kinetic energy widths are practically independent of the pulse energy. This can be easily understood: the pulse energy influences the probability

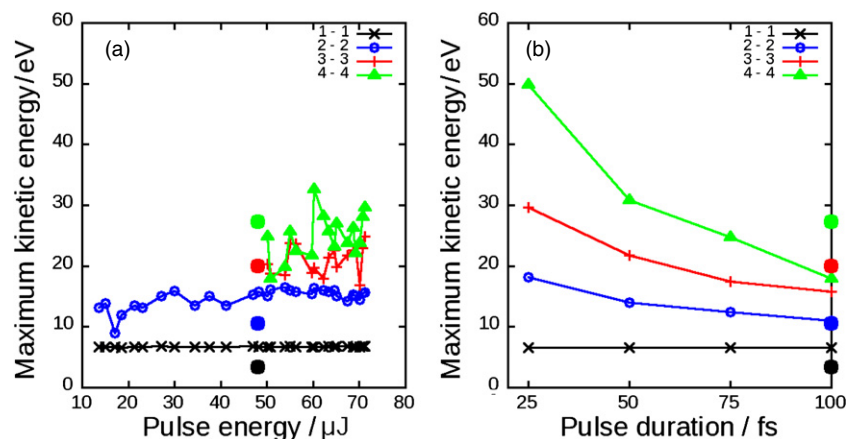


**Figure 11.** Simulated variation in the maximum fragment kinetic energy of  $N_2$  Coulomb explosion as a function of (a) the FEL pulse energy (assuming a 100 fs pulse duration and the focal conditions described in the experimental section), (b) the FEL pulse duration (assuming the experimental pulse energy distribution and the focal conditions described in the experimental section). Large filled circles show experimental results at  $48 \mu\text{J}$  average pulse energy and 100 fs expected pulse duration. The discrepancies between the experiment and the simulation are discussed in the text.

of the explosion, but not its dynamics, which are governed by the pulse duration. This is further revealed in figure 11(b), where the distribution widths are plotted for four different assumed pulse durations from 25 to 100 fs (with the latter number corresponding to our present experiment). One can immediately see that the widths are strongly dependent on the pulse duration, and are increasing towards shorter pulses. This is because for short pulses, multiple sequential ionization happens earlier in the course of the explosion, when the internuclear distance is smaller and therefore leads to higher potential energies available for the ionic fragments.

The robustness of the kinetic energy distribution widths against varying the pulse energy and their sensitivity to the pulse duration suggests that the scaling of figure 11(b) can provide estimates for unknown pulse durations of XUV lasers. In this method, the covariance mapping technique would be a vital part of the analysis, because detailed charge-selected kinetic energy distributions need to be extracted to determine the pulse durations. In the same experiment, charge-state population distributions can be determined in order to measure the actual XUV peak intensity in the focus, thus making covariance mapping a powerful tool for the diagnostics of XUV laser beams.

The results presented in figures 6, 8 and 9 convincingly demonstrate that the simulations reproduce the main features of the Coulomb explosion for the case of nitrogen. Apart from the 1–1 island, the momentum distributions in figure 9 are correctly predicted by consideration of the classical dynamics of a system of two nitrogen atoms. The deviations for the 1–1 channel can be attributed to dissociation on the  $N_2^+$  potential energy surface, which is neglected in the present simulation.

The covariance map in figure 5 reveals a covariance island for ions  $I^{8+}$ – $I^{9+}$ . The observation of this channel was unexpected, because formation of  $I^{9+}$  ions requires not only removal of all 5s and 5p electrons, but the additional removal of two 4d electrons. The available energy of 91 eV is not enough to produce  $I^{9+}$  from the  $I^{7+}$ – $I^{8+}$  channel. The observation of this channel can probably be opened by the resonance-enabled

x-ray multiple ionization (REXMI) mechanism [30–32], where transient resonant excitation enhances the ionization process beyond the limit expected by the straightforward sequential ionization model. Alternatively, it can be explained by a shake-up process during one of the preceding ionization steps, which would leave weakly bound electrons in excited states. Such electrons can later be removed by the 91 eV photon ionization, albeit with very low cross sections. One other possibility is that this channel arises from ionization of molecules by the third harmonic of the FEL pulse, which is known to be transmitted [33, 34]. However, the rather low third harmonic content of 0.5% [34] to 2% [33] and the low ionization cross section at this photon energy (about 0.75 Mb [29]) renders this explanation less likely.

## 7. Conclusions

In conclusion, recording single-shot ion TOF spectra for the ionization of  $N_2$  and  $I_2$  molecules by intense XUV pulses at the FLASH FEL and a subsequent analysis of the data using a partial covariance mapping technique allows the extraction of momentum distributions for all significant Coulomb explosion channels. The comparison of the extracted data with simulations suggests that Coulomb explosion of  $N_2$  molecules is well described by a model with two atoms moving on classical trajectories, and with minimal corrections for molecular effects. This suggests that  $N_2$  molecules and their Coulomb explosion can be used as a robust tool for the assessment of unknown parameters of pulsed XUV sources, such as the light intensity in the focus and the pulse durations.

In contrast, the case of  $I_2$  presents a challenge, because multi-electron effects such as Auger decay and shake-up seem to be important. The data on  $I_2$  reveal the presence of  $I^{8+}$  and  $I^{9+}$  ions via their correlation to the  $I^{7+}$  and  $I^{8+}$  Coulomb explosion partners. In a picture of sequential electron removal from the ground state, the formation of the  $I^{9+}$  ions by single-photon absorption is forbidden, since the photon energy is insufficient. This raises questions on the role of REXMI

or shake-up processes in multi-photon ionization of iodine molecules, but can also be due to higher order harmonics of the XUV light transmitted by FEL.

## Acknowledgments

Portions of this research were carried out at the light source facilities FLASH at DESY. DESY is a member of the Helmholtz Association (HGF). We would like to thank Rolf Treusch for assistance in using beam line BL2 at FLASH. In addition we would like to thank the FLASH staff. KU is grateful to Ministry of Education, Culture, Sports, Science and Technology of Japan for support of the X-Ray Free Electron Laser (XFEL) Utilization Research Project and the XFEL Priority Strategy Program. LJF thanks the EPSRC, UK (grants no. EP/F021232/1, EP/F034601/1 and EP/I032517/1). PJ would like to acknowledge the support of the Swedish Research Council and the Swedish Foundation for Strategic Research. Financial support by the Marie Curie Research Training Networks ATTOFEL is gratefully acknowledged. The authors are grateful to Christian Schröter, Thomas Schultz and Robin Schöneberg for assistance with preparation of the experiments.

## References

- [1] Ackermann W *et al* 2007 Operation of a free-electron laser from the extreme ultraviolet to the water window *Nature Photon.* **1** 336
- [2] Shintake T *et al* 2008 A compact free-electron laser for generating coherent radiation in the extreme ultraviolet region *Nature Photon.* **2** 555
- [3] Emma P *et al* 2010 First lasing and operation of an angstrom-wavelength free-electron laser *Nature Photon.* **4** 641
- [4] Ishikawa T *et al* 2012 A compact x-ray free-electron laser emitting in the sub-ångström region *Nature Photon.* **6** 540
- [5] Neutze R, Wouts R, van der Spoel D, Weckert E and Hajdu J 2000 Potential for biomolecular imaging with femtosecond x-ray pulses *Nature* **406** 752
- [6] Chapman H N *et al* 2006 Femtosecond diffractive imaging with a soft-x-ray free-electron laser *Nature Phys.* **2** 839
- [7] Redecke L *et al* 2013 Natively inhibited *Trypanosoma brucei* Cathepsin B structure determined by using an x-ray laser *Science* **339** 227
- [8] Boutet S *et al* 2012 High-resolution protein structure determination by serial femtosecond crystallography *Science* **337** 362
- [9] Seibert M M *et al* 2011 Single mimivirus particles intercepted and imaged with an x-ray laser *Nature* **470** 78
- [10] Chapman H N *et al* 2011 Femtosecond x-ray protein nanocrystallography *Nature* **470** 73
- [11] Quiney H M and Nugent K A 2011 Biomolecular imaging and electronic damage using x-ray free-electron lasers *Nature Phys.* **7** 142
- [12] Ullrich J, Moshhammer R, Doerner A, Schmidt L P H and Schmidt-Böcking H 2003 Recoil-ion and electron momentum spectroscopy: reaction-microscopes *Rep. Prog. Phys.* **66** 1463
- [13] Jiang Y H *et al* 2009 Few-photon multiple ionization of  $N_2$  by extreme ultraviolet free-electron laser radiation *Phys. Rev. Lett.* **102** 123002
- [14] Yamada A *et al* 2010 Ion-ion coincidence studies on multiple ionizations of  $N_2$  and  $O_2$  molecules irradiated by extreme ultraviolet free-electron laser pulses *J. Chem. Phys.* **132** 204305
- [15] Eppink A T J B and Parker D H 1997 Velocity map imaging of ions and electrons using electrostatic lenses: application in photoelectron and photofragment ion imaging of molecular oxygen *Rev. Sci. Instrum.* **68** 3477
- [16] Rosca-Pruna F *et al* 2001 Spatial alignment of diatomic molecules in intense laser fields. I: experimental results *J. Phys. B: At. Mol. Opt. Phys.* **34** 4919
- [17] Springate E *et al* 2001 Spatial alignment of diatomic molecules in intense laser fields. II: numerical modelling *J. Phys. B: At. Mol. Opt. Phys.* **34** 4939
- [18] Johansson P *et al* 2008 Velocity map imaging of atomic and molecular processes at the free electron laser in Hamburg (FLASH) *J. Mod. Opt.* **55** 2693
- [19] Rouzee A *et al* 2011 Angle-resolved photoelectron spectroscopy of sequential three-photon triple ionization of neon at 90.5 eV photon energy *Phys. Rev. A* **83** 031401
- [20] Frasiniski L J, Codling K and Hatherly P A 1989 Covariance mapping—a correlation method applied to multiphoton multiple ionization *Science* **246** 1029
- [21] Frasiniski L J, Giles A J, Hatherly P A, Posthumus J H, Thompson M R and Codling K 1996 Covariance mapping and triple coincidence techniques applied to multielectron dissociative ionization *J. Electron Spectrosc. Relat. Phenom.* **79** 367–71
- [22] Sorokin A A *et al* 2006 Method based on atomic photoionization for spot-size measurement on focused soft x-ray free-electron laser beams *Appl. Phys. Lett.* **89** 221114
- [23] Fraser G W 2002 The ion detection efficiency of microchannel plates (MCPs) *Int. J. Mass Spectrom.* **215** 13
- [24] Meier R and Eberhardt P 1993 Velocity and ion species dependence of the gain of microchannel plates *Int. J. Mass Spectrom.* **123** 19
- [25] Eder H, Vana M, Aumayr F and Winter H P 1997 Precise total electron yield measurements for impact of singly or multiply charged ions on clean solid surfaces *Rev. Sci. Instrum.* **68** 165
- [26] Vana M, Kurz H, Winter H P and Aumayr F 1995 Potential and kinetic electron emission from clean gold induced by multicharged nitrogen ions *Nucl. Instrum. Methods Phys. Res. B* **100** 402
- [27] Krzanowski W J 1988 *Principles of Multivariate Analysis* (New York: Oxford University Press) chapter 14.4
- [28] Franceschi P, Ascenzi D, Tosi P, Thissen R, Žabka J, Roithová J, Ricketts C L, De Simone M and Coreno M 2007 Dissociative double photoionization of  $N_2$  using synchrotron radiation: appearance energy of the  $N^{2+}$  dication *J. Chem. Phys.* **126** 134310
- [29] Los Alamos Atomic Codes <http://aphysics2.lanl.gov/cgi-bin/ION/runlanl08d.pl>
- [30] Rudek B *et al* 2012 Ultra-efficient ionization of heavy atoms by intense x-ray free-electron laser pulses *Nature Photon.* **6** 858
- [31] Rudek B *et al* 2013 Resonance-enhanced multiple ionization of krypton at an x-ray free-electron laser *Phys. Rev. A* **87** 023413
- [32] Motomura K *et al* 2013 Sequential multiphoton multiple ionization of atomic argon and xenon irradiated by x-ray free-electron laser pulses from SACLA *J. Phys. B: At. Mol. Opt. Phys.* **46** 164024
- [33] Johansson P, Siu W, Gijsbertsen A, Meijer A S, van der Zande W J, Verhoeven J and Vrakking M J J 2007 Single-shot harmonic content measurements and velocity map imaging at the FLASH free electron laser *HASYLAB Annual Report 2007* pp 445–6
- [34] Düsterer S *et al* 2006 Spectroscopic characterization of vacuum ultraviolet free electron laser pulses *Opt. Lett.* **31** 1750–2